# Stable Field Emission from Nanoporous Silicon Carbide

Myung-Gyu Kang[1,2], Henri Lezec[1], and Fred Sharifi[1]

[1]The Center for Nanoscale Science and Technology
National Institute of Standards and Technology
Gaithersburg, MD 20899-6204

[2]Maryland NanoCenter, University of Maryland
College Park, MD 20742

## Abstract

We report on a new type of stable field emitter capable of electron emission at levels comparable to thermal sources. Such an emitter potentially enables disruptive advances in several important technologies which currently use thermal electron sources. These include communications through microwave electronics, and more notably imaging for medicine and security where new modalities of detection may arise due to variable-geometry x-ray sources. Stable emission of 6 $A/cm^2$ is demonstrated in a macroscopic array, and lifetime measurements indicate these new emitters are sufficiently robust to be considered for realistic implementation. The emitter is a monolithic structure, and is made in a room-temperature process. It is fabricated from a silicon carbide wafer, which is formed into a highly porous structure resembling an aerogel, and further patterned into an array. The emission properties may be tuned both through control of the nanoscale morphology and the macroscopic shape of the emitter array.

## 1. Introduction

Field emission has been persistently researched for decades, and continuing advances in design and synthesis of new materials have significantly aided the development of cold electron sources [1-5]. This research is motivated by the distinct technological advantages enabled by

desirable properties of field-extracted electrons, compared to those that are thermally produced. Attributes such as reduced beam spread and fast response time would allow for disruptive improvements in a broad array of applications including displays [2], microwave electronics [6], and x-ray sources [7,8]. These may respectively lead to increased energy efficiency, superior communication and radar, and new imaging capabilities for medicine and security. All of these applications require an emitter that is reliable and capable of producing the desired emission current; more critically, the latter two require high emission currents that so far have only been in the realm of thermal sources. Here, we report on a new type of field emitter with performance which may potentially enable use in these technologies.

Whereas in thermionic emission electrons are released through heat, field emission extracts electrons using an applied electric field through quantum mechanical tunneling. Electron field emission is described by the Fowler-Nordheim model [9] in which the tunneling barrier is distorted by the large applied electric field. The electron current density $J$, is expressed as

$$J = \frac{k_1 \beta^2 E^2}{\phi} \exp(-k_2 \frac{\phi^{1.5}}{\beta E})$$

where $k_1$ and $k_2$ are constants dependent on the properties of the barrier. The current density is exponentially dependent on the emitter's work function $\phi$, the applied electric field $E$, and the magnitude of field enhancement caused by the shape of the emitter $\beta$. For arrays of emitters, $\beta$ is defined by a two level hierarchy: 1) the local electric field enhancement at the level of the individual emitter, set by the size and shape of the local nanostructure, and 2) the global electric field enhancement, set by the larger scale spatial arrangement of the emitters comprising the array. Numerous technologies have been pursued to increase field enhancement at the first level,

ranging from early conically-shaped tip approaches [1], and more recent efforts focused on carbon nanotubes with continuing reports of improved performance [10].

Here, we demonstrate control of this two-level field enhancement hierarchy in these emitters. These structures are fabricated from highly n-doped silicon carbide wafers which are electrochemically etched into a continuous and highly porous structure. These are subsequently formed by ion etching into a variety of arrays, while maintaining morphology and porosity, as shown in Figure 1 and Movies 1 and 2. At the local level, field enhancement is defined by the shape of the nanostructure, and varied through electrochemistry conditions so as to alter relevant features such as porosity and wall thickness. At the second level, the macroscopic shape of the emitter array establishes the global field enhancement across the emission area. The starting material, silicon carbide, is chosen as it is refractory and capable of withstanding high current densities. It also possesses a wide bandgap and these wafers are heavily n-doped. The two properties lead to increased emission by reducing the work function through enhanced electron affinity, as the tunneling process is dominated by electrons in the upper conduction band.

## 2. Experiment

Wafers of 6-H poly-type, with nominal resistivity ranging from 0.02 Ω·cm to 0.2 Ω·cm were etched into porous structures, detailed in Appendix. We have explored a range of electrochemical conditions, and the resulting structures are dependent on the specifics of the anodization chemistry. This difference in nanostructure morphology manifests itself in the emission characteristics, as it leads to different local field enhancement. As an example, Figures 2a and 2b demonstrate the variation in structure that results from wafers anodized using electrochemical solutions with different conductivity. In the first (Condition 1), the etching

conditions produce structures with wide variations in pore size, and pore wall thickness ranging from 30 nm to 200 nm, where the thicker pore walls dominate the structure (Figure 2a). In the second (Condition 2), more oriented structures with smaller wall thickness were produced, with typical pore sizes of 150 nm and wall thickness between 20 nm and 30 nm (Figure 2b).

These surface emitters were tested in a large-area diode configuration described in Appendix. As field enhancement requires high aspect ratio structures, the thinner average pore walls of wafers processed through Condition 2 should ideally lead to higher emission. This is indeed observed as shown in Figure 2c, where the emission characteristics corresponding to the two conditions are plotted. (For comparison, testing was also performed on an unprocessed wafer, demonstrating no significant emission.)

Further field enhancement may be achieved through design of the larger scale structure of the emitting array. For this goal, a variety of exploratory structures were fabricated to assess the mechanical robustness and the limits of aspect ratio that could be achieved (Figure 1). The anodized structures were initially plasma-etched into macroscopic mesas (Figure 1b) and formed into shaped arrays using lithographically defined etch masks, or through a high resolution focused ion beam (FIB). Compared to the original mesa, the area is reduced by 85 % for the fin array (Figure 1c), and 96 % for the pillar array (Figure 1d). The fin and pillar arrays were formed from a starting square mesa (Figure 1b) with a lateral dimension more than ten-fold the pitch or the height of the emitter, detailed in Appendix. This relative scaling is important for the measured current density to accurately represent larger sized arrays, and thus be macroscopic. Thus all current densities reported here are calculated using the macroscopic dimensions of the emitter array, defined by the lateral dimensions of the starting mesa.

## 3. Results and discussion

In contrast to the surface emitters formed solely by wafer anodization (Figures 2a, 2b), electron emission in the patterned structures occurs at lower electric fields, and is initially dominated by emission from the array's perimeter due to this region's higher electric field enhancement. In the test procedure, the field is increased until the current density from this perimeter region exceeds the material's inherent capability (discussed below), at which point the emission drops as the nanostructure becomes compromised. Consequently, the perimeter field is diminished, the array emits more uniformly across the entire structure, and the current continues to rise with increasing electric field. Since this emission is now over a larger area, significant stable emission may be obtained, and the fields required to reach the material limit in this regime are higher. Figures 3a-d detail the perimeter and areal emission characteristics of a mesa (Figure 1b) and a pillar array (Figure 1d), demonstrating this effect. Post-testing scanning electron microscopy at various stages of test indicates the likely failure mechanism is a morphology change in the structure (Figure 1f). It is manifested as rounding of the nanostructure surface suggesting decomposition of the silicon carbide. Our results indicate the emission is stable so long as the material's inherent limit is not exceeded. Finally, in Figure 4 the areal emission characteristics of the mesa, fin, and pillar arrays (Figures 1b-d) are shown, demonstrating the second level field enhancement arising from the global structure of the array. We note the pillar array (Figure 1d) produced stable emission in excess of 6 $A/cm^2$ at 7.5 V/μm, a value that compares favorably with carbon nanotube emitters [10], and is at the level of standard thermal sources [11].

Several lifetime and reliability measurements have been undertaken to ascertain the robustness of these structures. We have performed both continuous pulse and dc testing, and the

results indicate (areal) emission is robust so long as the current densities remain below where material decomposition occurs. For our experimental configuration, the fields required to reach this material limit may be readily obtained for the pillar array (Figure 1d). As shown in Figure 4c (inset), the emission fluctuates and becomes unstable at a current density above 7 A/cm$^2$, and post-test SEM examination indicated material decomposition (Figure 1f).

To assess reliability at high current densities below the decomposition point, a mesa emitter was repeatedly subjected to a slow dc ramping of the electric field detailed in Figure 3b, and showed no changes over an hour's operational time. Further, testing has also been performed on mesh arrays with 30 % of the area of the starting mesa (Figure 1e). This structure was subjected to sequences of dc pulses of applied voltage, each pulse approximately 5 seconds long, with varying off times between each pulse (60 sec, 100 sec, and 200 sec). As shown in Figure 5a, the emission does not vary as long as the emitter is allowed sufficient time (200 sec) to cool to its original temperature, and shows only a slight increase in emission within the pulse duration (Figure 5a, inset). As the off-time is decreased to 100 sec and 60 sec and the emitter temperature is allowed to rise (Figure 5b, 5c), the overall emission increases accordingly and the enhancement within a pulse is more pronounced. The results show the dc emission levels consistently exceed 1 A/cm$^2$ during this demanding test protocol. At the highest current densities, local heating resulted in the emitter exhibiting a faint reddish glow during the pulse. The emitters recover to initial levels once allowed to cool. This test procedure also resulted in an overall emission time of approximately an hour.

**4. Conclusion**

With further optimization of materials and process, the promising performance reported in these initial studies raises the realistic possibility of field emitters as a potential replacement

for thermal sources. We believe the robustness is partly due to the monolithic nature of the structures, as there are no material interfaces that may be potential failure points. In addition, the porous morphology leads to a continuous supply of emission points as the emitting surface wears. Both should prove to be advantageous for performance and reliability. We are cautiously optimistic performance characteristics may be further enhanced through improvements of electrochemistry conditions and geometric design, towards realization of an effective cold cathode technology capable of producing high current.

**Acknowledgements**

The authors thank Dr. Rachel Cannara for numerous insightful discussions. M.-G. K. acknowledges support under the Cooperative Research Agreement between the University of Maryland and the National Institute of Standards and Technology, the Center for Nanoscale Science and Technology, through Award 70NANB10H193.

**Appendix**

*Fabrication*: The porous silicon carbide structures tested were produced by electrochemical etching using two processing conditions, and are similar to a previous report [12]. In Condition 1, the anodizing solution consisted of 10 % HF and 5 % ethanol (by mass) with balance distilled water. In Condition 2, the anodization solution consisted of 20 % HF and 5 % ethanol (by mass) with balance de-ionized water. Ohmic contact to the backside (silicon-face) of the wafer was formed using Ni (50 nm), annealed at 300 C in Ar. The etched side (carbon-face) is subsequently anodized at 20 V using a Pt mesh counter-electrode, at a nominal rate of 4 μm/min. The use of de-ionized water in Condition 2 resulted in a dense top layer approximately 2 μm in

thickness with low porosity. This top layer was subsequently removed by reactive ion etching (RIE) using 90 % $SF_6$ and 10 % $O_2$ plasma etching, exposing an underlying structure with more uniform porosity and smaller wall thickness than wafers anodized using Condition 1.

The structure shown in Figures 1b is a square mesa 210 μm per side. It was fabricated through the formation of the nanoporous structure on a SiC wafer, and subsequently patterned with a metal etch mask through conventional photolithography, and RIE etched as before. This mesa fabrication procedure was also used for fabrication of the fin and pillar arrays shown in Figures 1c,d. Here, the mesas were further patterned by FIB etching (Ga+ ions, 30 keV beam energy, 2.5 nA beam current, 50 nm nominal beam diameter) assisted by $XeF_2$ gas. Compared to FIB milling without gas, the use of gas-assisted etching (GAE) in shaping emitters in porous SiC leads to a significant increase in material removal rate (by a factor of ~6). In Figure 1c, the fins comprising the array are 1.5 μm wide, 20 μm high, at 10 μm pitch. In Figure 1d, the square pillars are 2 μm per side and 20 μm high, with the same pitch. In Figure 1e, the mesh structure array is 0.5 mm per side, and has hexagon sides 10 μm long, 2.3 μm wide, and 20 μm high, fabricated by the RIE process outlined above.

*Testing and Analysis:* The test apparatus is parallel-plate geometry in a vacuum chamber with a base pressure of 1.3 x $10^{-7}$ Pa, and testing was typically initiated at 1 x $10^{-6}$ Pa. The anode and cathode are 1 cm in diameter. The electrode separation is controlled precisely as it determines the electric field value, and is typically at 1.000 mm ± 0.002 mm. The measurements were performed either in sequential dc or pulse mode, with pulse widths ranging from 0.2 ms to 10 ms and a typical frequency of 1 Hz. The emission results were independent of the pulse widths. The pulse data shown in Figures (2c, 3a, 3c, 3d, 4b, 4c) were obtained using a 0.2 ms square pulse at a frequency of 1 Hz. The uncertainty in electric field is 0.2 %, (1σ) and is determined

by the uncertainties in the electrode separation and output of the high voltage apparatus. The uncertainty in the emission current is 0.1 % ($1\sigma$) and is determined by the precision of the current measurement apparatus. For the extraction of $\beta$ through F-N data analysis, the values used for the constant of integration and work function are $k_2 = 6.83 \times 10^7$ eV$^{-3/2}$·V·cm$^{-1}$ and $\phi =$ 4.2 eV respectively.

**References**


[1] Spindt C A 1968 *J. Appl. Phys*. **39,** 3504-5

[2] de Heer W A, Châtelain A and Ugarte D 1995 *Science* **270,** 1179-80

[3] Fan S, Chapline M G, Franklin N R, Tombler T W, Cassell A M and Dai H 1999 *Science* **283,** 512-4

[4] Hsu D S Y and Shaw J 2002 *Appl. Phys. Lett.* **80,** 118-20

[5] Teo K B K, Minoux E, Hudanski L, Peauger F, Schnell J P, Gangloff L, Legagneux P, Dieumegard D, Amaratunga G A J and Milne W I 2005 *Nature* **437,** 968

[6] Jensen K L 1999 *Physics of Plasmas* **6,** 2241-53

[7] Wang G, Yu H and De Man B 2008 *Med. Phys.* **35,** 1051-64

[8] Schwoebel P R 2006 *Appl. Phys. Lett*. **88,** 113902

[9] Fowler R H and Nordheim L 1928 *Proc. R. Soc. London, Ser. A* **119,** 173-81

[10] Calderón-Colón X, Geng H, Gao B, An L, Cao G and Zhou O 2009 *Nanotechnology* **20,** 325707

[11] Cronin J L 1981 *IEE Proc.* **128,** 19-32

[12] Ke Y, Devaty R P and Choyke W J 2008 *Phys. Stat. Sol. (b)* **245,** 1396-403.

**Figure Captions**

**Figure 1.** Scanning electron microscopy (SEM) images of various porous SiC emitter structures. **a,** Pillar test structure patterned by FIB, scale bar: 10 μm. **b,** Mesa structure fabricated by photolithography and RIE, scale bar: 50 μm. **c,** Magnified view of fin array fabricated by FIB, scale bar: 4 μm. **d,** Pillar arrays fabricated by FIB, scale bar: 50 μm. **e,** Hexagonal mesh arrays fabricated by photolithography and RIE, scale bar: 10 μm. **f,** Pillar structure demonstrating change in morphology due to material decomposition. The inset shows the surface prior to test, scale bar: 1 μm.

**Figure 2.** Top SEM images of electrochemically etched wafer using two different conditions and the measured current densities (J) vs. applied electric field (E). **a,** Conditions 1, scale bar: 1μm. **b,** Condition 2, scale bar: 1μm. **c,** Resulting J vs. E curves for Conditions 1 and 2, and an unprocessed wafer.

**Figure 3.** J vs. E and corresponding Fowler-Nordheim (FN) plots (inset) of the mesa and pillar structures. **a,** Initial emission tests dominated by the perimeter of a mesa. **b,** Stable areal emission characteristics of the same mesa. For **b** six different J vs. E data sets were measured at various electrode separations ranging from 0.24 mm to 1.35 mm. In each curve, the voltage was continuously ramped to the maximum value and then decreased, in increments of 20 V steps every 0.5 seconds. **c,** Initial tests of a pillar array, dominated by perimeter emission. **d,** Stable areal emission of the same pillar array. The FN inset shows the extracted $\beta$ values.

**Figure 4.** J vs. E plots of patterned structures showing emission enhancement through macroscopic geometric design of the emitter array for a mesa (Figure 1b), fin (Figure 1c)**,** and pillar (Figure 1d) array. The turn on fields, defined for a current of 10 μA, are 4.4 V/μm, 6.5 V/μm, and 9.6 V/μm for the pillar, fin, and mesa structures respectively. Inset **c**: J vs. E extended to the failure point of the pillar array, demonstrating emission instability (red) as the material limit is reached.

**Figure 5.** Emission vs. pulse number for testing of the mesh structure shown in Figure 1e. Each pulse is five seconds in duration. The off times in the pulse sequence are not shown to ease comparison between results. The off times are 200 sec, 100 sec, and 60 sec for figure a, b, and c, respectively. The insets show the emission profile during a pulse, at the end of the pulse sequence (denoted by "*"); time intervals in the insets are one second.

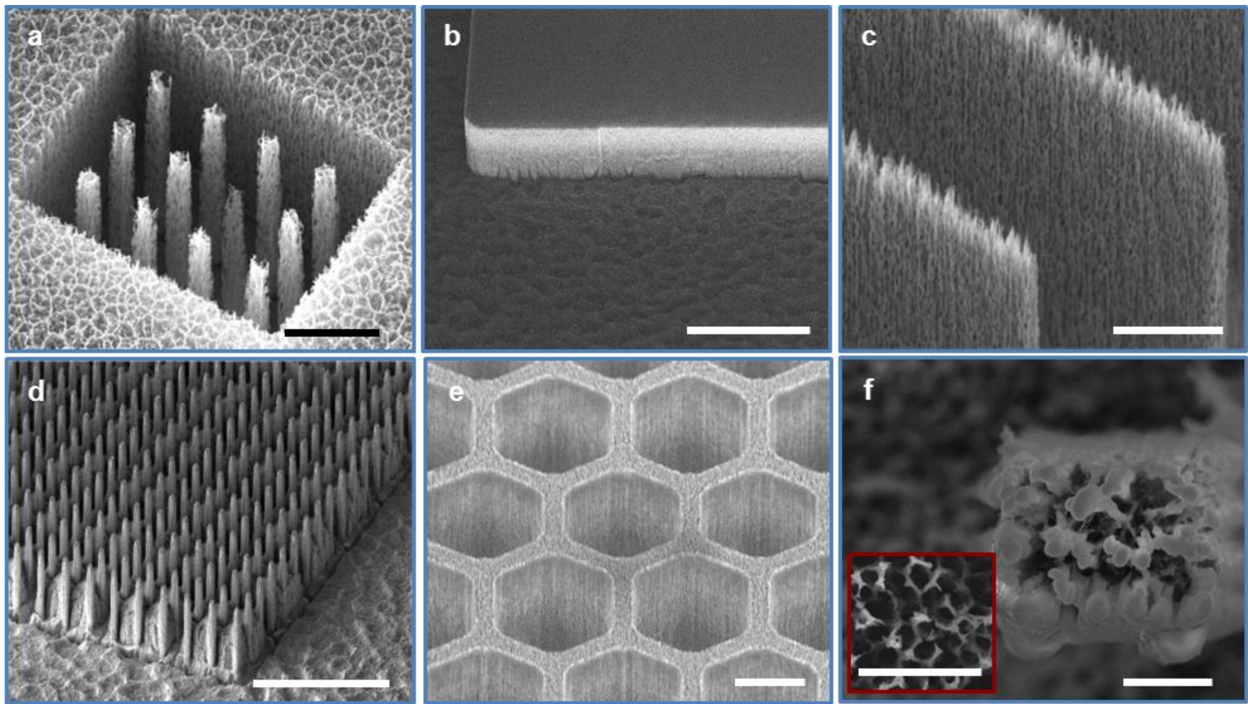


Figure 1

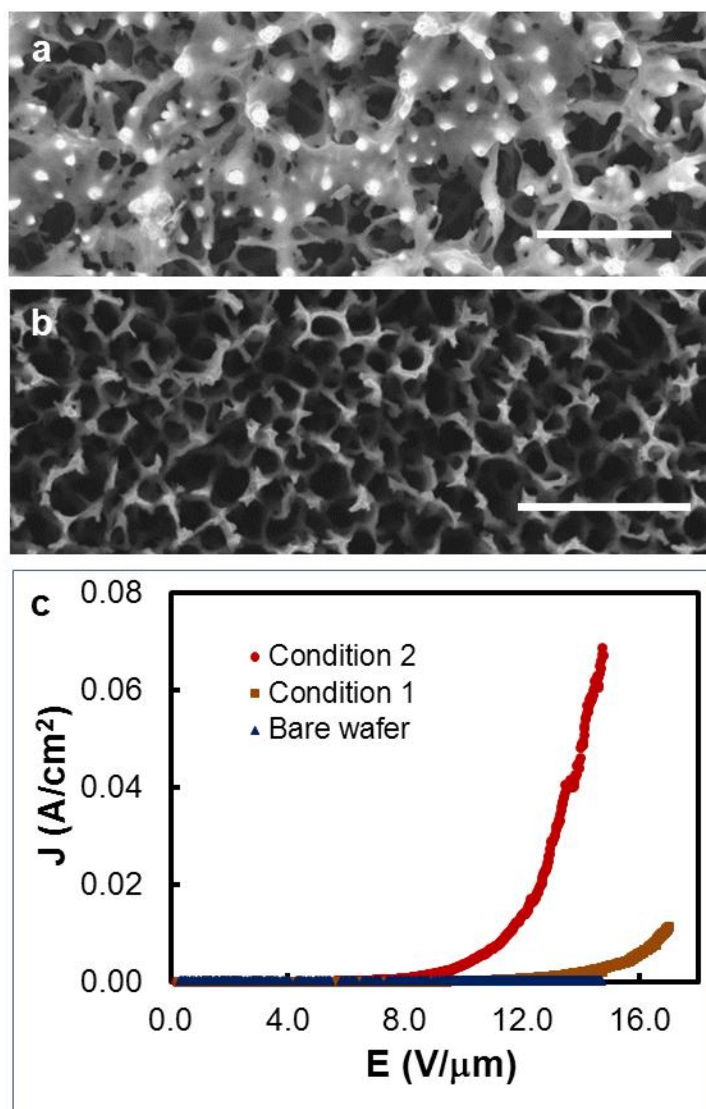


Figure 2

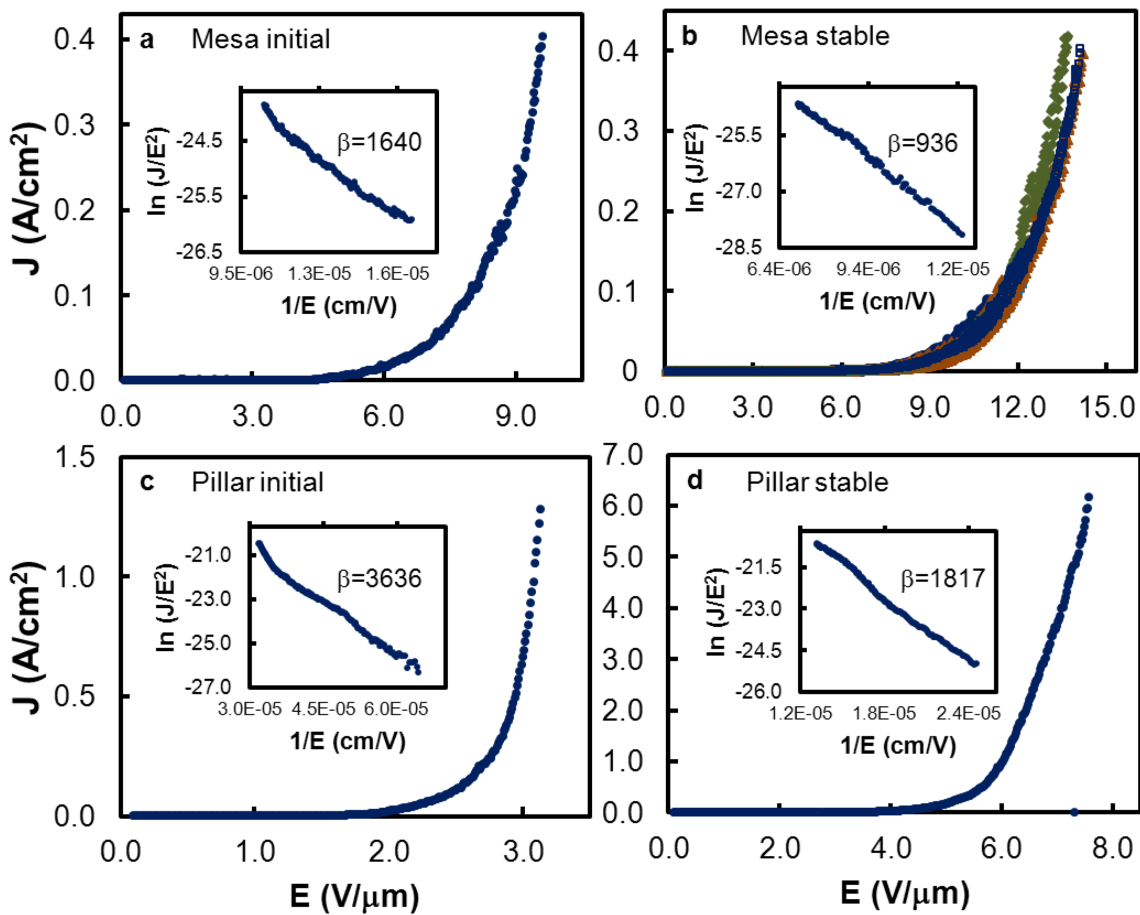


Figure 3

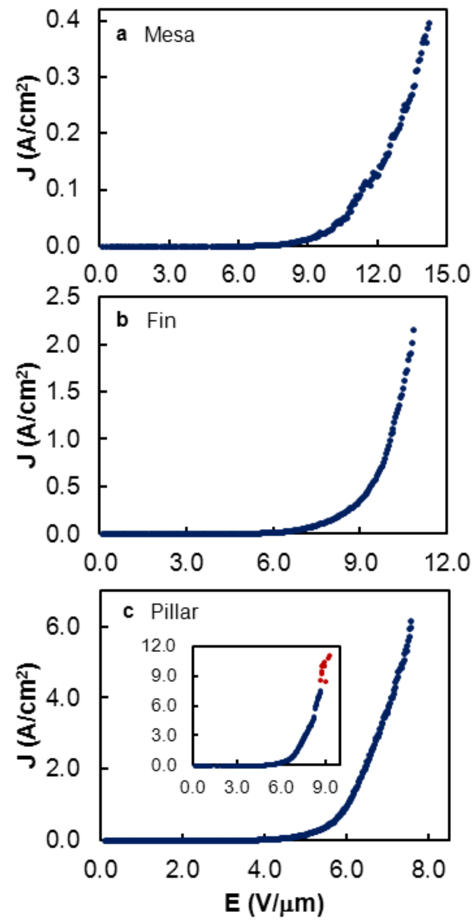


Figure 4

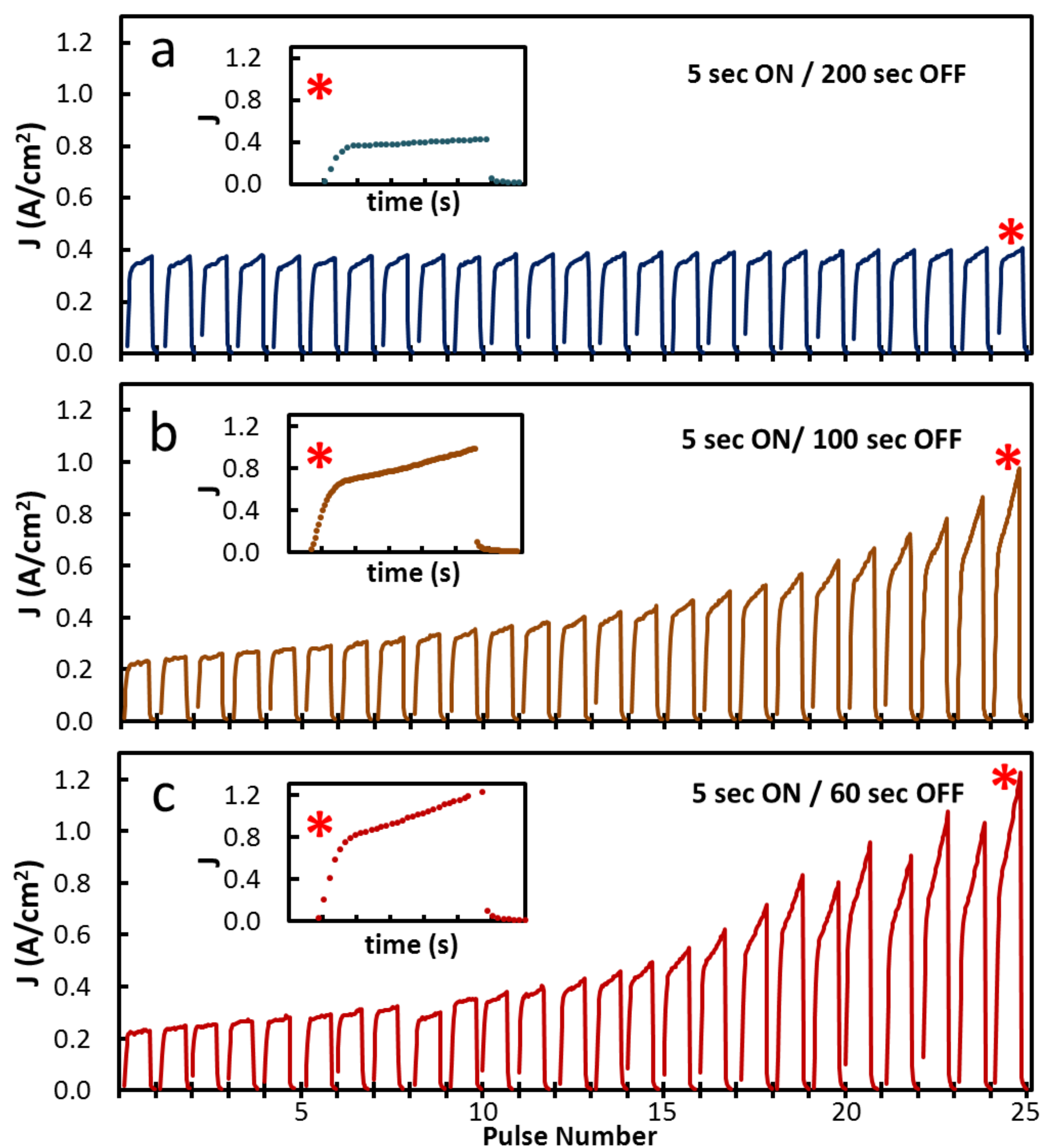


Figure 5